Title
Ultrahigh Hot Carrier Transient Photocurrent in Nanocrystal Arrays by Auger Recombination.

Journal
Nano letters, 19(7)

ISSN
1530-6984

Authors
Gao, Jianbo
Kidon, Lyran
Rabani, Eran
et al.

Publication Date
2019-07-01

DOI
10.1021/acs.nanolett.9b02374

Peer reviewed

Ultra-High Hot Carrier Transient Photocurrent in Nanocrystals Arrays by Auger Recombination

Jianbo Gao,[§,1,2 †] Lyran Kidon, [§,1,3] Eran Rabani,[*1,3,4] and A. Paul Alivisatos[*1,2,3,5]

[1]*Department of Chemistry, and* [2]*Department of Materials Science and Engineering, University of California, Berkeley, Berkeley, California 94720, United States*
[3]*Materials Sciences Division, Lawrence Berkeley National Laboratory, Berkeley, California 94720, United States*
[4]*The Raymond and Beverly Sackler Center for Computational Molecular and Materials Science, Tel Aviv University, Tel Aviv, Israel 69978*
[5]*Kavli Energy NanoScience Institute, University of California, Berkeley and Lawrence Berkeley National Lab, Berkeley, California 94720, United States*

[§]J.G. and L. K. contributed equally to this work.
[†]Present address: Department of Physics and Astronomy, Ultrafast Photophysics of Quantum Devices Laboratory, Clemson University, South Carolina 29634, United States
Corresponding Authors: *E-mail: paul.alivisatos@berkeley.edu; eran.rabani@berkeley.edu

In this report, we show that a new mechanism for carrier transport in solution-processed colloidal semiconductor nanocrystal arrays exists at high excitation intensity on ultra-fast timescales, and allows for facile intrinsic transport between as-prepared nanocrystals over long distances. By combining a high speed photoconductive switch with an ultra-fast laser excitation in a sub-40 ps photoconductor, we observed *transient* photocurrents with peak densities of $3 \bullet 10^4 - 10^6 \mathrm{mA/cm^2}$ in self-assembled PbSe nanocrystals capped with long native oleic acid ligands. The ratio between the transient photocurrent peak and the steady-state dark current is ten orders of magnitude. The *transient* mobility at the peak current is estimated to range between $0.5 - 17.5 cm^2/Vs$ for the various nanocrystal sizes studied, which is 6 to 9 orders of magnitude higher than the dark current steady-state mobility in PbSe, CdSe, and CdTe nanocrystals capped with native ligands. The results are analyzed using a kinetic model which

attributes the ultra-high transient photocurrent to multiple photo-generated excitons undergoing on-particle Auger recombination, followed by rapid tunneling at high energies. This mechanism is demonstrated for a wide range of PbSe nanocrystals sizes (diameters from $2.7\,\mathrm{nm}$ to $7.1\,\mathrm{nm}$) and experimental parameters. Our observations indicate that native ligand-capped nanocrystal arrays are promising for optoelectronics applications wherein multiple carriers are photo-injected to inter-band states.

Keywords: nanocrystals, native ligands, ultrafast, hot carrier, Auger recombination, tunneling, transport

Electrical transport in colloidal nanocrystal arrays has advanced remarkably over the last decade.[1] Today it is possible to prepare transistors,[2] solar cells,[3,4] light emitting diodes,[5] and photodetectors with solution process methods,[6,7] with performance that continues to improve markedly. One unifying challenge in these studies is how to assure strong coupling and facile transport between nanocrystals.[8-10] One established approach to improve carrier transport is to replace the long native ligands during wet chemistry synthesis with shorter organic or inorganic ligands, thereby enhancing inter-nanocrystal coupling. However, such surface treatments typically introduce high densities of defect states or mid-gap states, leading to a significant reduction of the modulation ratio in transistors (with gate bias/ without gate bias ¿10^5) and photoconductivity (photocurrent/dark-current ¿10).[8,10,11] Here we show that the intrinsic inter-nanocrystal transport is transiently dramatically altered at high carrier density, because multi-exciton effects create a new pathway for efficient hot carrier transport, similar to that proposed by Efros and collaborators.[12] This observation

demonstrates that today's nanocrystals can be used to study many interesting transient intrinsic transport and collective phenomena in the high carrier density regime in artificial solids built from colloidal nanocrystals.

Pioneering studies by Klimov,[13,14] Nozik,[15,16] Bawendi,[17] and others have revealed the rich transient behavior that occurs when small colloidal nanocrystals are excited by strong fields, generating more than a single exciton per nanocrystal. The resulting multiple excitons interact strongly, dramatically altering the energy levels as well as the radiative and nonradiative rates of relaxation. Such effects have often been attributed to limiting the practical uses of nanocrystals, as is the case for lasing,[13] where enhanced Auger multiexciton nonradiative pathways make it harder to achieve population inversion. Such multiexciton effects need not be detrimental, of course, for instance they have been hypothesized to aid the power conversion in solar cells under certain conditions.[13] Here we illustrate clear evidence of how they can be useful for transient transport characteristics in arrays of assembled PbSe nanocrystals, and how precisely the same mechanism that makes colloidal nanocrystals turn dark at high excitation densities works in favor of improving the transient transport between the nanocrystals, making them ideal transient high-peak-power photoconductors.

In order to investigate the transient transport between colloidal nanocrystals in the high-energy density regime, we build on our recent practical demonstration of PbSe nanocrystal-based photoconductive switches[18-21] in which an array of nanocrystals can be addressed by two electrodes while retaining optical access for a high power ultrafast pulsed laser, providing a means to study the dynamics of excited charge carriers in the few tens of picoseconds after the nanocrystals are excited. PbSe nanocrystals with native oleic acid capping ligands in hexane

were spin-coated on a glass substrate to form a $1\ \mu m$ thick film (see Fig. 1A for TEM image), which was integrated into a coplanar transmission lines device structure to act as a high-speed photoresponse waveguide upon ultrafast laser excitation to form a photoconductive Auston switch (Fig. 1B). A sub-$40\ ps$ system response time was achieved (Fig. 1C). The fast time resolution is independent of the nanocrystal size, as well as active semiconductor material, indicating that the bandwidth of the instrument components (including coaxial cables, connectors, and sampling oscilloscope) is the limiting factor for the time resolution. Detailed nanocrystals, film, and device characterization are presented in the Supplementary Information (Fig. S1-S8).

A typical transient response under the photon flux of $4\ mJ/cm^2$ is shown in Fig. 1D, where a rapid increase in the transient photocurrent is followed by a slower decrease to values of dark current. The photocurrent density peak is shown to depend on the magnitude of the applied bias across the junction and ranges between $10^4 mA/cm^2$ and $10^6 mA/cm^2$. The transient peak value is ten orders of magnitude larger than the steady state dark current (Fig. 1E) and 6-9 orders of magnitude larger than the steady-state photocurrent in PbSe, CdSe or CdTe nanocrystals arrays capped with oleic acid and trioctylphosphine oxide (TOPO) ligands, respectively.[2, 5, 7, 22]

Figure 1| Typical device structure and ultrafast transient photocurrent characteristics. (A) Transmission electron microscopy (TEM) image of a representative PbSe nanocrystal array, featuring a $10\ nm$ scale bar. **(B)** Schematic of the photoconductive Austin switch. The Au electrode spacing is $25\ \mu m$ and the bright area indicates the laser illumination region onto the PbSe nanocrystal film. Inset: high resolution TEM of two representative PbSe nanocrystals, indicating that the inter nanocrystal distance is $\sim 3.0\ nm$. The scale bar is $5\ nm$. **(C)** The system response time (temporal difference between 10% and 90%) is sub-$40\ ps$. **(D)** Typical ultrafast

transient photocurrent dependence on the bias voltage applied. The $800\ \mathrm{nm}$ wavelength excitation laser has a flux of $4\ \mathrm{mJ/cm^2}$ illuminating the array of $5.4\ \mathrm{nm}$ diameter nanocrystals at $78\ \mathrm{K}$. **(E)** The peak transient photocurrent density and the dark current density as a function of voltage in the same device.

To reveal the fundamental mechanism of carrier photo-generation and transient transport which results in the observed ultra-high peak transient photocurrent density and high transient carrier mobility, we study the transient photocurrent dependence on the laser flux and temperature, as summarized in Fig. 2 for various nanocrystal sizes. The nanocrystal diameters range from $2.7\ \mathrm{nm}$ to $7.1\ \mathrm{nm}$, corresponding to a band gap energy E_g that spans between $1.2\ \mathrm{eV}$ to $0.65\ \mathrm{eV}$, respectively. All samples were excited with photon energy of $1.55\ \mathrm{eV}$. The excited carriers relax rapidly to the band edge on a picosecond timescale (unresolvable in our measurements).[23]

Figure 2| Typical laser flux and temperature dependence. (A) The peak transient photocurrent dependence on laser flux for various size nanocrystals spanning from $2.7\ \mathrm{nm}$ to $7.1\ \mathrm{nm}$ diameters, for a bias voltage of $V_{sd}=100\ \mathrm{V}$ and temperature $\mathrm{T} = 78\ \mathrm{K}$. The dashed line is the 4^{th} order power law for a guide. **(B)** Typical ultrafast photocurrent dependence with temperature ranging from $78\ \mathrm{K}$ to $300\ \mathrm{K}$, for a nanocrystal diameter of $4.1\ \mathrm{nm}$ and a bias voltage of $V_{sd}=100V$. The inset is the photocurrent peak and decay time dependence with temperature. Note that the oscillations are a result of impedance mismatch, which slightly varies with devices and do not correspond to an internal physical process. Similar oscillations were observed in reference GaAs photoconductive devices, shown in Supplementary Information (Fig. S7).

Fig. 2A shows a power law relation between the photocurrent peak and laser flux in a log-log scale with a slope that approximately equals four, indicating that within the initial detection time and for the limited range of incident laser intensity studied here, each nanocrystal contributing to the transient photocurrent in the photo-activated domain has an average of 4 excitons. The

four-photon absorption process is independent of nanocrystal size and is persistent within the limited experimental variation range of about three-fold in laser intensities studied, as indicated by Fig. 2A. Further discussion on the observed excitation density required to activate the observed transient phenomena is given in the Supplementary Information. We propose that the effect of the increase in laser intensity can be described simply by an increase in the photo-active domain (in which the excitation density is the same); higher laser flux results in the deeper penetration of the photons into the nanocrystal layer and an increase in the overall number of photo-excited nanocrystals.

The temperature dependence of the transient photocurrent is shown in Fig. 2B. We find that the rapid rise, the slow decay, and the magnitude of the peak (insets, Fig. 2B) are roughly temperature independent, although the photocurrent decay curves are slightly different at various temperatures. While the response itself depends on the nanocrystal size, a similar behavior with temperature was found for all sizes studied (Fig. S9). This suggests that photo-activated transient transport observed is governed by tunneling events rather than thermally activated hopping from one nanocrystal to another as in the dark current. The tunneling process therefore depends on the number of excitations produced initially and on the size of the nanocrystals (through the size dependence of the Auger recombination lifetime).[24]

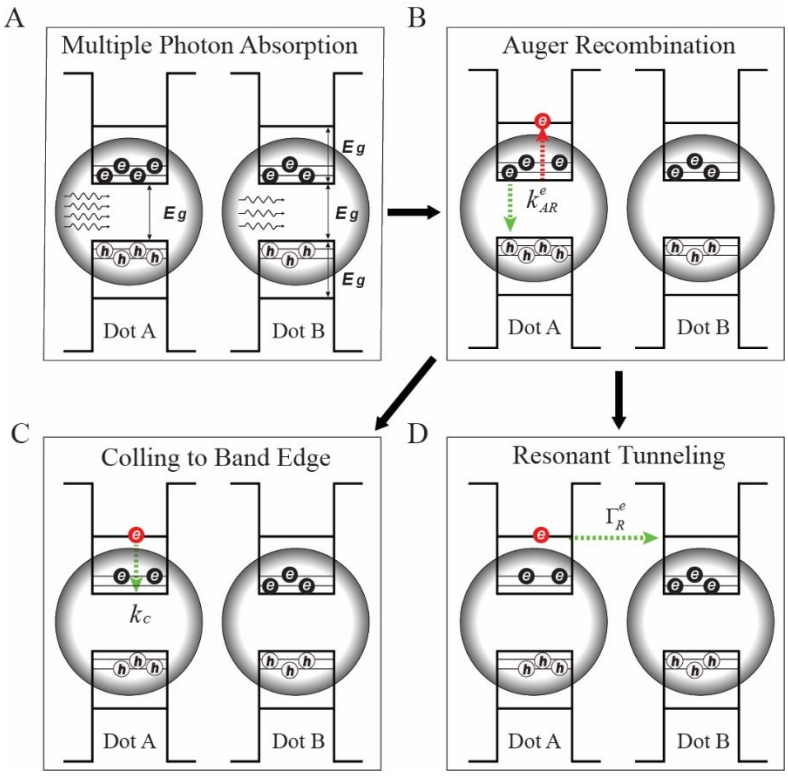

Figure 3| Carrier photogeneration and transport model. **(A)** Initially, each nanocrystal contains several band-edge excitons distributed according to the Poisson distribution. **(B)** These multiple excitons recombine non-radiatively via an Auger process ($k_{AR}^{e/h}$) to promote charge carriers to higher energies. Electron is an example to demonstrate the one band gap promotion. **(C)** The excited charge carriers can decay back to the band edge, with a timescale given by the phonon emission rate, k_C or **(D)** tunnel to a neighboring nanocrystal with a rate $\Gamma_{L/R}^{e/h}$ (see text for the mathematical expressions of all rates).

We propose a kinetic scheme to explain the experimental observations, sketched in Fig. 3. Initially, several electron-hole pairs generated by the laser flux relax rapidly to the band edge (Fig. 3A) on a sub-picosecond timescale.[25] We assume that the number of such pairs in each nanocrystal within the photo-activated domain is distributed according to the Poisson distribution, which was well-documented by various groups such as Klimov, Beard, and Siebbeles.[13,14,26-28] In

our case, the mean exciton pair value $\lambda=4$ (consistent with the experimental observation in Fig. 2A).

The charge carriers can tunnel to the nearest neighbor nanocrystal, but the band-edge tunneling is rather slow for several reasons: (a) The band-edge states of the nearest neighbor nanocrystal are filled by other carriers, blocking any transition due to Pauli repulsion, (b) inhomogeneities in size of nanocrystals along with a discrete density of accepting states (due to the quantum confinement effect) imply off-resonant conditions, and (c) the tunneling matrix element is rather small due to the large barrier and large distance between nanocrystals. Thus, we neglect altogether tunneling of carriers at the band-edge, consistent with previous measurements[2,5,7,22] where the photocurrent of the band-edge carriers was 6-9 orders of magnitude smaller than the peak transient photocurrent observed here.

The band edge carriers can recombine radiatively on a very long timescale (several nanoseconds) or recombine nonradiatively via an Auger process to generate hot carriers at higher quasiparticle energy level (reducing the number of carriers by two). In this case, the excited carrier energy is one band gap above the conduction band edge (Fig. 3B). The Auger recombination rate depends on the number of carriers. For nanocrystals in the strong confinement limit where interaction between the carriers can be ignored to lowest order in the Coulomb couplings, the Auger rate can be expressed as $k_{AR}^{e}=\frac{1}{2}n_e\left(n_e-1\right)n_h k_T^e$ for the electrons and $k_{AR}^{h}=\frac{1}{2}n_h\left(n_h-1\right)n_e k_T^h$ for the holes,[13,14,24] where n_e/n_h are the

number of electrons/holes at the band edge for each nanocrystal, and k_T^e/k_T^h is the negative/positive trion annihilation rate, both scale roughly with the volume of the nanocrystal.[24] Only one carrier takes the excess energy (E_g) released by the recombination of an electron-hole pair across the bandgap, while the others remain spectators at the band edge. The mechanism up to this point is similar to that proposed by the Efros group,[12] with one important difference – the band gap and ionization energies in the nanocrystals studied here do not allow for carrier auto-ionization, but instead the hot carriers remain somewhat localized in the nanocrystal (see Fig. S11 in the Supplementary Information and discussion around it).

Carriers that are injected to energies E_g above the conduction band minimum or below the valance band maximum can undergo two processes. First, they can relax to the band edge by phonon emission, with a rate given by the cooling rate k_C (Fig. 3C). This occurs on timescales of ≈ 1.5 ps for PbSe nanocrystals[23,25] and is referred to as a "cooling process". In addition to the cooling process, excited carriers at high energy states can tunnel to neighboring nanocrystals (Fig. 3D). This tunneling process is much faster than the tunneling at the band edge for several reasons: (a) The carriers tunnel to neighboring nanocrystals at energies with low occupancy probability and thus are not blocked by Pauli repulsion, (b) the tunneling is on-resonance (off-resonance tunneling can also contribute, but requires coupling to phonon, and thus is slower), since the density of states at energies E_g above the conduction band minimum or below the valance band maximum is rather high and inhomogeneities do not play a significant role at these higher energies, and (c) the barrier for tunneling is lower than that for

band-edge carriers. Since measurements of the tunneling rate are difficult, we use a semi-classical (WKB) approximation for the tunneling rate (see Supplementary Information for more details).

We assume that tunneling only occurs between nanocrystals and ignore the dynamics of the carriers within the nanocrystals themselves. This assumption is valid for the strong quantum confinement limit, which is indeed the case for all nanocrystal sizes studied here.[29] The tunneling rates $\Gamma_{L/R}^{e/h}\left(D, V_{SD}\right)$ (L/R for tunneling to the Left/Right, e/h for electron/hole tunneling) are given by Fermi's golden rule:

$$\Gamma_{L/R}^{e/h}\left(D, V_{SD}\right)=\frac{2\pi}{\hbar}\left|V_{L/R}^{e/h}\left(D, V_{SD}\right)\right|^2 \rho_{e/h}\left(E_g\left(D\right)\right), \quad (0)$$

where $\rho_{e/h}\left(E\right)=\nu\frac{1}{2\pi^2}\left(\frac{2m_{e/h}^{*}}{\hbar^2}\right)^{3/2}\sqrt{E}$ is the density of states for the conduction (e)/valance (h) bands in energies in the low occupancy probability regime, with $\nu=\frac{\pi}{6}D^3$ the volume of the nanocrystal (D is the nanocrystal diameter), and $m_{e/h}^{*}$ the effective mass of the electron/hole ($m_e^{*}\approx 0.256\, m_e$ and $m_h^{*}\approx 0.145\, m_e$).[30] The coupling strengths, $V_{L/R}^{e/h}$, are difficult to compute or measure.[31] We model these as:

$$\left|V_{L/R}^{e/h}\left(D, V_{SD}\right)\right|^2=\left|\widetilde{V}\right|^2 \gamma_{L/R}^{e/h}\left(E_g\left(D\right), V_{SD}\right), \quad (2)$$

where $\widetilde{V}=1.5\, meV$ is assumed to be a constant, independent of the effective mass or size of the nanocrystal, and is the only fitting parameter used, with a single value for all fitted measurements. The voltage dependence is introduced

in the unitless factor, $\gamma_{L/R}^{e/h}\left(E_g(D), V_{SD}\right)$, which is given by (see Supplementary Information for more details):

$$\frac{\gamma_L^{e/h}\left(E_g(D), V_{SD}\right)}{\gamma_R^{e/h}\left(E_g(D), V_{SD}\right)} = \frac{\exp\left(\frac{-2}{\hbar}\delta D\sqrt{2\, m_{e/h}^{*}\left(V_0 \pm \delta V\left(V_{SD}, D\right) - E_g(D)\right)}\right)}{\exp\left(\frac{-2}{\hbar}\delta D\sqrt{2\, m_{e/h}^{*}\left(V_0 \mp \delta V\left(V_{SD}, D\right) - E_g(D)\right)}\right)}. \tag{3}$$

We use the Gillespie algorithm[32] to solve the nonlinear master equations for an array of $N_x \times N_y$ nanocrystals in 2D (see Supplementary Information for further information about the nonlinear master equations, the effective rates for each process and our use of the Gillespie algorithm). 5000 trajectories were used to average over the initial distribution of electron-hole pairs in the photo-activated domain. The coupling to the metallic contacts is modeled by a contact resistance with a tunneling time given by Γ_{cont} for both electrons and holes. We find that only electron-hole pairs near the contacts contribute significantly to the current. Furthermore, the peak of the transient photocurrent depends nearly linearly on the lateral dimension of the device (for both trends, see Fig. S12). This allows us to use a relatively small nanocrystal array ($N_x = 100, N_y = 10$) to converge the results. The interpretation of the dependence on the contact-to-contact distance is confirmed by mean path displacement calculations performed at zero bias, in which excitations were found to diffuse (on average) ~ 10 sites (see Fig. S13), corresponding to ~50-100 nm depending on the nanocrystal dimensions.

In Fig. 4 we analyze the timescales governing the photocurrent response. We find that the rise time is mainly determined by the response time of the device (we convolute the raw data from simulation with a Gaussian response of width $40\, ps$)

and the cooling rate (Fig. 4A). Larger cooling rates also result in a smaller peak value, since excited carriers lose energy before they can tunnel to the neighboring sites and contribute to the overall current. It is interesting to note that the cooling time that provides the best fit to the experimental transient photocurrent is also consistent with the experimental cooling rate measured directly (see inset of Fig. 4A)), which was subsequently used in all the following model simulations.

The long-time decay dynamics are analyzed in Fig. 4B. The long-time relaxation is governed by the slowest timescale in the system. In the experiments reported here, this corresponds to the timescale of tunneling between the sites in the array and the contacts (given by the contact tunneling rate), leading to a long-time decay that is independent of the size of nanocrystals. The asymptotic decay depends solely on the Auger recombination rate when $\Gamma_{cont} > k_{AR}^{e/h}$, but this limit is not observed in the experiments (see Figs. S14-S17).

Figure 4| Timescales. The dependence of the transient photocurrent on the cooling rate **(A)** and on the contact resistance **(B)** obtained from the master equations. The insets show the width of the photocurrent peak as a function of the cooling lifetime **(A)** and the asymptotic decay time as a function of the contact resistance rate **(B)**. The calculations were made for an array of $7\,\mathrm{nm}$ nanocrystals (for additional simulation parameters, see Table S2).

In Fig. 5 we show comparisons between the experimental and theoretical results for the transient photocurrent dependence on the laser flux and electrical field. Clearly, the model captures both the role of laser intensity as well as the effect of bias voltage. An increase in the right/left tunneling rates ratio given by Eq. (1) reproduces the effect of an increase in bias voltage, and an increase in the number of photo-activated sites reproduces the effect of increasing the laser

intensity. In comparing the theoretical results to the experiments, we have used the coupling strength $\widetilde{V}$ as the only fitting parameter, choosing a reasonable value in the 1 meV range (see Supplementary Information for more details). The other parameters were determined from previous experiments (cooling and Auger recombination rates)[24] or from the longtime decay of the experimental photocurrent governed by the contact resistance.

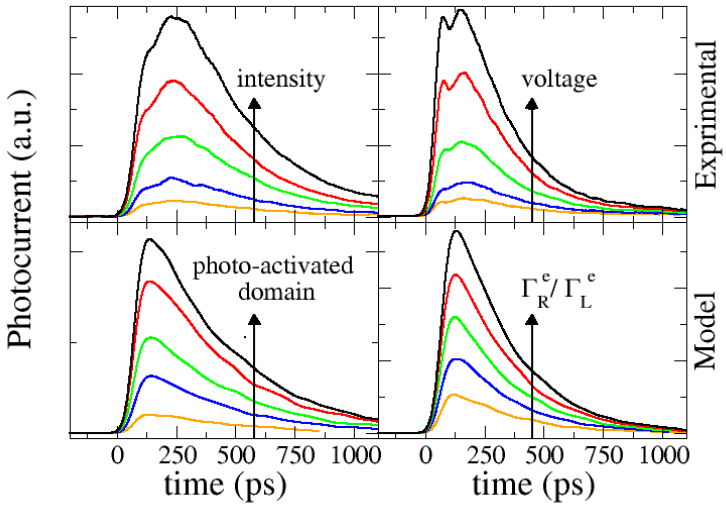

Figure 5| Recovering the experimental behavior. The dependence of the transient photocurrent on the laser intensity (left panels) and on the bias voltage (right panels). Upper panel are the experimental results for a $7\,\mathrm{nm}$ nanocrystals array at $\mathrm{T}=300\ \mathrm{K}$, and lower panels are simulation results with parameters $k_c=0.66\,ps^{-1}$ and $k_T^{e/h}=0.009\,ps^{-1}$, corresponding to a $7\,\mathrm{nm}$ nanocrystal. The contact tunneling rates are determined from the decay of the corresponding experimental photocurrent, $k_{cont}=3\times10^{-3}\,\mathrm{ps}^{-1}$ (bottom left panel) and $k_{cont}=4.5\times10^{-3}\,\mathrm{ps}^{-1}$ (bottom right panel). On the left, experimental dependence on laser flux ranging from $1.6\ \mathrm{mJ/cm}^2$ to $3.6\ \mathrm{mJ/cm}^2$ (top) is compared to simulation results for increasing photo-activated domains in the 2D case (bottom). On the right, dependence on bias voltage ranging from $10\,\mathrm{V}$ to $80\,\mathrm{V}$ (top) is compared to simulation results for increasing right/left tunneling rate ratios. For additional simulation parameters, see Table S2 in the Supplementary Information.

With the kinetic model shown to reproduce the experimental results, we can extract other physical quantities not directly accessible experimentally. Of

importance is the average transient mobility of the photo-generated carriers at the peak photocurrent. At low fields, consistent with the voltages applied in the experiment, the hot carrier transient mobility within the nanocrystal array can be defined as $\mu_{ex}^{e/h}=\langle \upsilon \rangle_{ex}^{e/h}/E$, where $\langle \upsilon \rangle_{ex}^{e/h}$ is the average velocity of the excited electrons/holes in the array and E is the electric field applied on the device (assumed uniform). This definition is similar to that used in steady-state linear-response measurements, however, since the transient photocurrent decays in time, so does the transient mobility of carrier. The time-dependent average velocity for all nanocrystal arrays follows the same pattern (see Figs. S18-S21): An extremely fast rise time (sub-picosecond) followed by a plateau, decaying exponentially to zero on the timescale of the Auger recombination lifetime. The transient mobility is shown to be bias independent (see Figs. S18-S21), consistent with the linear regime assumption. As a function of nanocrystal size (see Fig. S22), the transient mobility at the plateau region (where it evaluates solely the inter-nanocrystal tunneling events, and not the number of carriers available) ranges from $0.49 cm^2/Vs$ (for $2.7\,\mathrm{nm}$ nanocrystals) to $17.5\,\mathrm{cm}^2/\mathrm{Vs}$ (for $7\,\mathrm{nm}$ nanocrystals). The nanocrystal size dependence is due to the increase in tunneling rate (Fig. S10) as well as the increase in tunneling length with nanocrystal size. This strong dependence may be a result of the assumption made for the tunneling rates, taking the transition matrix element to be roughly size independent.

Notably, the above transient mobility values are about eight orders of magnitude higher than steady state mobilities previously reported for native ligand-capped PbSe nanocrystal arrays obtained by field effect transistor measurements (

$10^{-7} cm^2/Vs$).[2] This suggests that carrier tunneling at the band edge, characteristic of the dark current, is estimated to be about eight orders of magnitude slower than the effective rate observed here. This is in full agreement with electronic structure calculations performed for a CdSe nanocrystal, showing that when the energy of the carriers approaches E_g above the conduction band minimum (below the valence band maximum), the carrier density outside the nanocrystal increases dramatically and is over 4 orders of magnitude larger than that of carriers at the band edge at ~ 1 nm away from the nanocrystal surface (see Fig. S11 in the Supplementary Information and discussion thereafter). Similar values for the steady state mobility have been observed, but only for doped nanocrystal arrays where some of the semiconductor nanocrystals have been exchanged by metal nanoparticles.

In summary, this study shows that the strong interaction between excitons in colloidal nanocrystals naturally produces high tunneling current between nanocrystals in an array, the precise inverse of the limits it imposes on light emission. The light-matter interaction between a strong ultrafast laser with a high electric field with strongly quantum confined materials enables direct, unambiguous observation of an extremely large peak transient photocurrent density, resulting from multiple exciton recombination exciting carriers to excited quasiparticle states, and leading to resonant tunneling transport with a high transient carrier mobility at these high-energy states. To this end, transient off resonant electric fields of laser light may be used to gate the carrier transport in nanocrystals arrays, providing means to switch high currents in electronic circuits at terahertz (THz) frequency, and possibly enabling innovative optoelectronic

technologies for data processing.[33] Furthermore, colloidal nanocrystals can be used as artificial atoms to investigate intrinsic transport mechanisms in artificial solids.

Supplementary Information

(1) Materials and Methods: PbSe Synthesis, PbSe nanocrystal optical and structure properties characterization (Fig. S1), PbSe nanocrystal film structure properties characterization (Figs. S2-S5), device fabrication and characterization (Figs. S6-S8); (2) Temperature dependence (Fig. S9); (3) Photon absorption characterization; (4) Model simulation – Methods and parametrization: nonlinear master equations (Table S1), calculation of the tunneling rates and (Figs. S10), the tunneling coupling matrix (Fig. S11), characterization of the 2D array simulation results (Fig. S12), analysis of average distance charge carriers transverse in the device (Fig. S13), simulation parameters (Table S2); (5) Reproducing the experimental behavior for different sized nanocrystals (Figs. S14-S17); (6) Transient mobility (Figs. S18-22).

Acknowledgments

This work was supported by the U.S. Department of Energy, Office of Science, Office of Basic Energy Sciences, Materials Sciences and Engineering Division, under Contract No. DE-AC02-05-CH11231 within the Physical Chemistry of Inorganic Nanostructures Program (KC3103). We thank Justin C. Ondry for help with TEM imaging.

Author Contributions

J.G. designed and performed the experiments. L.K. developed the theoretical model and carried out the model simulation. E.R. and A.P.A. supervised the

project and wrote the manuscript with J.G. and L.K. All authors discussed the results and commented on the manuscript.

Competing Financial Interests

The authors declare no competing financial interest.

References

1. Alivisatos, A. P. *Science* **1996,** 271, (5251), 933-937.
2. Talapin, D. V.; Murray, C. B. *Science* **2005,** 310, (5745), 86-89.
3. Semonin, O. E.; Luther, J. M.; Choi, S.; Chen, H. Y.; Gao, J. B.; Nozik, A. J.; Beard, M. C. *Science* **2011,** 334, (6062), 1530-1533.
4. Huynh, W. U.; Dittmer, J. J.; Alivisatos, A. P. *Science* **2002,** 295, (5564), 2425-2427.
5. Dai, X. L.; Zhang, Z. X.; Jin, Y. Z.; Niu, Y.; Cao, H. J.; Liang, X. Y.; Chen, L. W.; Wang, J. P.; Peng, X. G. *Nature* **2014,** 515, (7525), 96-99.
6. Konstantatos, G.; Howard, I.; Fischer, A.; Hoogland, S.; Clifford, J.; Klem, E.; Levina, L.; Sargent, E. H. *Nature* **2006,** 442, (7099), 180-183.
7. Sukhovatkin, V.; Hinds, S.; Brzozowski, L.; Sargent, E. H. *Science* **2009,** 324, (5934), 1542-1544.
8. Kagan, C. R.; Murray, C. B. *Nat Nanotechnol* **2015,** 10, (12), 1013-1026.
9. Dolzhnikov, D. S.; Zhang, H.; Jang, J.; Son, J. S.; Panthani, M. G.; Shibata, T.; Chattopadhyay, S.; Talapin, D. V. *Science* **2015,** 347, (6220), 425-428.
10. Kovalenko, M. V.; Scheele, M.; Talapin, D. V. *Science* **2009,** 324, (5933), 1417-1420.
11. Lee, J. S.; Kovalenko, M. V.; Huang, J.; Chung, D. S.; Talapin, D. V. *Nat Nanotechnol* **2011,** 6, (6), 348-352.
12. Shabaev, A.; Efros, A. L.; Efros, A. L. *Nano Lett* **2013,** 13, (11), 5454-5461.
13. Klimov, V. I. *Annu Rev Conden Ma P* **2014,** 5, 285-316.
14. Pietryga, J. M.; Park, Y. S.; Lim, J. H.; Fidler, A. F.; Bae, W. K.; Brovelli, S.; Klimov, V. I. *Chem Rev* **2016,** 116, (18), 10513-10622.
15. Ellingson, R. J.; Beard, M. C.; Johnson, J. C.; Yu, P. R.; Micic, O. I.; Nozik, A. J.; Shabaev, A.; Efros, A. L. *Nano Lett* **2005,** 5, (5), 865-871.
16. Nozik, A. J.; Beard, M. C.; Luther, J. M.; Law, M.; Ellingson, R. J.; Johnson, J. C. *Chem Rev* **2010,** 110, (11), 6873-6890.
17. Klimov, V. I.; Mikhailovsky, A. A.; Xu, S.; Malko, A.; Hollingsworth, J. A.; Leatherdale, C. A.; Eisler, H. J.; Bawendi, M. G. *Science* **2000,** 290, (5490), 314-317.
18. Auston, D. H.; Johnson, A. M.; Smith, P. R.; Augustiniak, W. M.; Bean, J. C.; Harbison, J. P.; Kaplan, D. *J Opt Soc Am* **1980,** 70, (6), 605-606.
19. Gao, J. B.; Fidler, A. F.; Klimov, V. I. *Nat Commun* **2015,** 6.
20. Fidler, A. F.; Gao, J. B.; Klimov, V. I. *Nat Phys* **2017,** 13, (6), 604-610.
21. Gao, J. B.; Nguyen, S. C.; Bronstein, N. D.; Alivisatos, A. P. *Acs Photonics* **2016,** 3, (7), 1217-1222.
22. Colvin, V. L.; Schlamp, M. C.; Alivisatos, A. P. *Nature* **1994,** 370, (6488), 354-357.
23. Franceschetti, A.; An, J. M.; Zunger, A. *Nano Lett* **2006,** 6, (10), 2191-2195.

24. Padilha, L. A.; Stewart, J. T.; Sandberg, R. L.; Bae, W. K.; Koh, W. K.; Pietryga, J. M.; Klimov, V. I. *Accounts Chem Res* **2013,** 46, (6), 1261-1269.
25. Schaller, R. D.; Pietryga, J. M.; Goupalov, S. V.; Petruska, M. A.; Ivanov, S. A.; Klimov, V. I. *Phys Rev Lett* **2005,** 95, (19).
26. Beard, M. C. *J Phys Chem Lett* **2011,** 2, (11), 1282-1288.
27. Aerts, M.; Sandeep, C. S. S.; Gao, Y. A.; Savenije, T. J.; Schins, J. M.; Houtepen, A. J.; Kinge, S.; Siebbeles, L. D. A. *Nano Lett* **2011,** 11, (10), 4485-4489.
28. Sandeep, C. S. S.; Ten Cate, S.; Schins, J. M.; Savenije, T. J.; Liu, Y.; Law, M.; Kinge, S.; Houtepen, A. J.; Siebbeles, L. D. A. *Nat Commun* **2013,** 4.
29. Lipovskii, A.; Kolobkova, E.; Petrikov, V.; Kang, I.; Olkhovets, A.; Krauss, T.; Thomas, M.; Silcox, J.; Wise, F.; Shen, Q.; Kycia, S. *Appl Phys Lett* **1997,** 71, (23), 3406-3408.
30. Kang, I.; Wise, F. W. *J Opt Soc Am B* **1997,** 14, (7), 1632-1646.
31. Nienhaus, L.; Wu, M. F.; Geva, N.; Shepherd, J. J.; Wilson, M. W. B.; Bulovic, V.; Van Voorhis, T.; Baldo, M. A.; Bawendi, M. G. *Acs Nano* **2017,** 11, (8), 7848-7857.
32. Gillespie, D. T. *J Phys Chem-Us* **1977,** 81, (25), 2340-2361.
33. Krausz, F.; Stockman, M. I. *Nat Photonics* **2014,** 8, (3), 205-213.

For TOC only